

LETTER TO THE EDITOR

# Direct estimation of electron density in the Orion Bar PDR from mm-wave carbon recombination lines <sup>★</sup>

S. Cuadrado<sup>1</sup>, P. Salas<sup>2</sup>, J. R. Goicoechea<sup>1\*\*</sup>, J. Cernicharo<sup>1</sup>, A. G. G. M. Tielens<sup>2</sup>, and A. Báez-Rubio<sup>3</sup>

<sup>1</sup> Instituto de Física Fundamental (IFF-CSIC). Calle Serrano 121-123, E28006 Madrid, Spain

<sup>2</sup> Leiden Observatory, Leiden University, P.O. Box 9513, NL-2300 RA Leiden, The Netherlands

<sup>3</sup> Centro de Astrobiología (CSIC-INTA), Ctra. de Torrejón a Ajalvir, km 4, E28850 Torrejón de Ardoz, Madrid, Spain

Received 27 March 2019 / Accepted 16 April 2019

## ABSTRACT

**Context.** A significant fraction of the molecular gas in star-forming regions is irradiated by stellar UV photons. In these environments, the electron density ( $n_e$ ) plays a critical role in the gas dynamics, chemistry, and collisional excitation of certain molecules.

**Aims.** We determine  $n_e$  in the prototypical strongly irradiated photodissociation region (PDR), the Orion Bar, from the detection of new millimeter-wave carbon recombination lines (mmCRLs) and existing far-IR [<sup>13</sup>C II] hyperfine line observations.

**Methods.** We detect 12 mmCRLs (including  $\alpha$ ,  $\beta$ , and  $\gamma$  transitions) observed with the IRAM 30 m telescope, at  $\sim 25''$  angular resolution, toward the H/H<sub>2</sub> dissociation front (DF) of the Bar. We also present a mmCRL emission cut across the PDR.

**Results.** These lines trace the C<sup>+</sup>/C/CO gas transition layer. As the much lower frequency carbon radio recombination lines, mmCRLs arise from neutral PDR gas and not from ionized gas in the adjacent H II region. This is readily seen from their narrow line profiles ( $\Delta v = 2.6 \pm 0.4$  km s<sup>-1</sup>) and line peak velocities ( $v_{\text{LSR}} = +10.7 \pm 0.2$  km s<sup>-1</sup>). Optically thin [<sup>13</sup>C II] hyperfine lines and molecular lines – emitted close to the DF by trace species such as reactive ions CO<sup>+</sup> and HOC<sup>+</sup> – show the same line profiles. We use non-LTE excitation models of [<sup>13</sup>C II] and mmCRLs and derive  $n_e = 60 - 100$  cm<sup>-3</sup> and  $T_e = 500 - 600$  K toward the DF.

**Conclusions.** The inferred electron densities are high, up to an order of magnitude higher than previously thought. They provide a lower limit to the gas thermal pressure at the PDR edge without using molecular tracers. We obtain  $P_{\text{th}} \geq (2-4) \cdot 10^8$  cm<sup>-3</sup> K assuming that the electron abundance is equal to or lower than the gas-phase elemental abundance of carbon. Such elevated thermal pressures leave little room for magnetic pressure support and agree with a scenario in which the PDR photoevaporates.

**Key words.** Astrochemistry - surveys - ISM: photon-dominated region (PDR) - ISM H II regions ISM: clouds

## 1. Introduction

Much of the mass and most of the volume occupied by molecular gas in star-forming regions lies at low visual extinction ( $A_V < 6$ , e.g., Pety et al. 2017). This means that, in the vicinity of OB-type massive stars, a significant fraction of the molecular gas is irradiated by relatively intense UV photon fluxes (e.g., Goicoechea et al. 2019). The interface layers between the hot ionized gas and the cold molecular cloud are photodissociation regions (PDRs; Hollenbach & Tielens 1999). PDRs host the critical H<sup>+</sup>/H/H<sub>2</sub> and C<sup>+</sup>/C/CO transition layers of the interstellar medium (ISM). Far-UV (FUV) photons with  $E < 13.6$  eV permeate molecular clouds, ionizing atoms, molecules, and dust grains of lower ionization potential (IPs). One signature of FUV-irradiated gas is an ionization fraction, defined as the abundance of electrons with respect to H nuclei ( $x_e = n_e/n_H$ ), higher than about  $10^{-6}$ . Cold molecular cores shielded from external FUV radiation show much lower ionization fractions,  $x_e \lesssim 10^{-8}$ , as the abundance of electrons is driven by the gentle flux of cosmic-ray particles rather than penetrating stellar FUV photons (Guelin et al. 1982; Caselli et al. 1998; Maret & Bergin 2007; Goicoechea et al. 2009).

Electrons play a fundamental role in the chemistry and dynamics of the neutral interstellar gas (meaning neutral atomic or

molecular hydrogen, but not ionized). The electron density ( $n_e$ ) controls the preponderance of ion-neutral reactions, i.e., the main formation route for many ISM molecules (Herbst & Klemperer 1973; Oppenheimer & Dalgarno 1974). The ionization fraction also controls the coupling of matter and magnetic fields. In addition, in high  $x_e$  environments, the large cross sections for inelastic collisions of electrons with certain high-dipole molecules such as HCN provide an additional source of rotational excitation (Goldsmith & Kauffmann 2017). In these cases, the observed molecular line emission is no longer controlled by the most abundant collisional partner, H<sub>2</sub>. Hence, the actual value of  $n_e$  affects how gas densities are estimated.

A direct determination of  $n_e$  in molecular clouds is usually not possible and we have to rely on indirect methods such as the observation of molecular ions and chemical modeling. In FUV-illuminated environments, electrons are supplied by the photoionization of abundant elements such as carbon and sulfur (both with IP < 13.6 eV), and also by the photoelectric effect on dust grains and polycyclic aromatic hydrocarbon (PAH) molecules (Bakes & Tielens 1994). In diffuse and translucent clouds, and at the FUV-irradiated edges of dense molecular clouds, most electrons arise from the ionization of carbon atoms. Carbon recombination lines (CRLs), in which a free electron recombines with carbon ions (C<sup>+</sup>) and cascades down from Rydberg electronic states to the ground while emitting photons, are expected to arise from neutral gas close to the C<sup>+</sup>/C/CO transition layer (e.g., Natta et al. 1994) and not from the hot

<sup>★</sup> Based on observations obtained with the IRAM 30 m telescope supported by INSU/CNRS (France), MPG (Germany), and IGN (Spain).

<sup>\*\*</sup> Corresponding author, e-mail: javier.r.goicoechea@csic.es

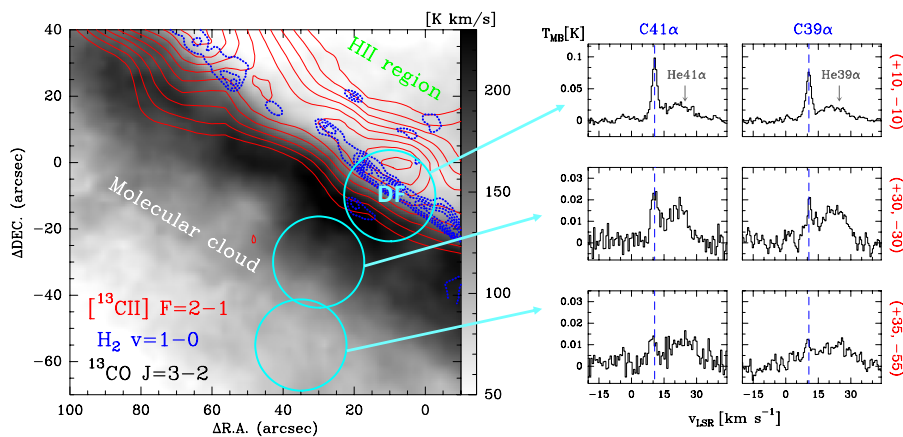


**Fig. 1.** Detection of mmCRLs toward the Orion Bar PDR. *Left:* Map of the  $^{13}\text{CO } J=3-2$  integrated emission obtained with the IRAM 30 m telescope at a HPBW of  $8''$  (Cuadrado et al., in prep.). The blue dashed contours show the position of the  $\text{H}_2$  dissociation front traced by the  $\text{H}_2 v=1-0 S(1)$  emission (from  $1.5$  to  $4.5 \cdot 10^{-4} \text{ erg s}^{-1} \text{ cm}^{-2} \text{ sr}^{-1}$  in steps of  $0.5 \cdot 10^{-4} \text{ erg s}^{-1} \text{ cm}^{-2} \text{ sr}^{-1}$ ; from Walmsley et al. 2000). Red contours show the  $[^{13}\text{C II}] (^2P_{3/2} - ^2P_{1/2}, F=2-1)$  line emission at  $1900.466 \text{ GHz}$  mapped with Herschel/HIFI at a HPBW of  $12''$  (from  $10$  to  $30 \text{ K km s}^{-1}$  in steps of  $2.5 \text{ K km s}^{-1}$ ; from Goicoechea et al. 2015). *Right:*  $\text{C}41\alpha$  and  $\text{C}39\alpha$  recombination lines detected with the IRAM 30 m telescope toward three positions of the PDR. The cyan circles roughly represent the HPBW of our 3 mm-wave observations.

(electron temperature  $T_e \approx 10,000 \text{ K}$ ) ionized gas in the adjacent  $\text{H II}$  region. This is readily seen from the narrower CRLs profiles compared to the broad H and He recombination lines ( $\Delta v \geq 20 \text{ km s}^{-1}$ , e.g., Churchwell et al. 1978). This conclusion is also in line with photoionization models where, in  $\text{H II}$  regions, carbon is mainly in the form of higher ionization states (e.g.,  $\text{C}^{++}$ ) (Rubin et al. 1991; Kaufman et al. 2006).

The  $^2P_{3/2} - ^2P_{1/2}$  fine-structure emission of singly ionized carbon (IP =  $11.3 \text{ eV}$ ), the famous  $[\text{C II}] 158 \mu\text{m}$  line, is bright and often shows an intensity linearly proportional to the  $\text{C}^+$  column density (the so-called effectively thin emission regime; Goldsmith et al. 2012). However, the line reaches moderate opacities toward bright and dense PDRs such as the Orion Bar (e.g., Ossenkopf et al. 2013; Goicoechea et al. 2015). Carbon recombination lines are optically thin (see Sect. 4) with an intensity proportional to  $n_e^2 T_e^{-2.5}$ . Although much fainter, mmCRLs can be observed from ground-based telescopes and can be used to infer  $n_e$  and  $T_e$  in FUV-irradiated neutral gas (Pankonin & Walmsley 1978; Salgado et al. 2017; Salas et al. 2018). CRLs have historically been detected at very low radio frequencies (e.g., at  $\sim 43 \text{ MHz}$  for  $\text{C}539\alpha$  or  $\sim 8.6 \text{ GHz}$  for  $\text{C}91\alpha$ ). Pushing to higher frequencies (i.e., lower principal quantum numbers  $n$ ) greatly improves the angular resolution of the observation even with single-dish telescopes. This allows us to access much smaller spatial scales and, potentially, to spatially resolve the narrow  $\text{C}^+/\text{C}/\text{CO}$  gas transition layer.

In this work we present the detection of several  $\alpha$  ( $\Delta n = 1$ ),  $\beta$  ( $\Delta n = 2$ ), and  $\gamma$  ( $\Delta n = 3$ ) mmCRLs ( $\text{C}n\Delta n$ ) observed from  $\sim 85 \text{ GHz}$  to  $\sim 115 \text{ GHz}$  toward the strongly FUV-irradiated ( $G_0 \geq 10^4$ ) PDR, the Orion Bar. This is a nearly edge-on interface of the Orion molecular cloud (OMC-1) with the ‘Huygens’ dense  $\text{H II}$  region, photoionized by young massive stars in the Trapezium cluster (e.g., Tielens et al. 1993; O’Dell 2001; Goicoechea et al. 2016; Pabst et al. 2019). Using the Effelsberg 100 m telescope, Natta et al. (1994) previously detected the  $\text{C}91\alpha$  line toward several positions of the irradiated surface of OMC-1. The same line was mapped with the VLA along the Bar by Wyrowski et al. (1997). They showed that the  $\text{C}91\alpha$  emission basically coincides with the emission in the  $v=1-0 S(1)$  line from vibrationally excited molecular hydrogen

( $\text{H}_2^*$ ). Most models of the Bar use  $n_e = 10 \text{ cm}^{-3}$  for the edge of the PDR (e.g., van der Tak et al. 2012, 2013). This value implies relatively low gas densities ( $n_{\text{H}} \approx 10^5 \text{ cm}^{-3}$ ) and thermal pressures in the CRL emitting layers, and through the PDR if the classical constant-density PDR model is adopted. The newly detected mmCRLs allow us to determine  $n_e$  and  $T_e$ , and to independently estimate the gas thermal pressure. This provides additional insights into the PDR structure and dynamics.

## 2. Observations and data reduction

We used the IRAM 30 m telescope at Pico Veleta (Sierra Nevada, Spain) to observe the Orion Bar in the mm band. We employed the E0 EMIR receiver ( $80 \text{ GHz} - 116 \text{ GHz}$ ) and fast Fourier transform spectrometer (FFTS) backend at  $200 \text{ kHz}$  spectral resolution ( $0.7 \text{ km s}^{-1}$  at  $90 \text{ GHz}$ ). These observations are part of a complete line survey ( $80 \text{ GHz} - 360 \text{ GHz}$ ; Cuadrado et al. 2015, 2016, 2017) toward a position close to the  $\text{H}_2$  dissociation front (DF; the  $\text{H}/\text{H}_2$  transition layer), almost coincident with what is known as the  $\text{CO}^+$  emission peak (Stoerzer et al. 1995). Here we present results obtained from deep observations in the 3 mm band toward three positions across the PDR (see Fig. 1). Their offsets with respect to  $\alpha_{2000} = 05^{\text{h}} 35^{\text{m}} 20.1^{\text{s}}$ ,  $\delta_{2000} = -05^{\circ} 25' 07.0''$  are  $(+10'', -10'')$  = DF,  $(+30'', -30'')$ , and  $(+35'', -55'')$ . In order to avoid the extended emission from OMC-1, we employed the position switching observing procedure with a reference position at offset  $(-600'', 0'')$ .

The half power beam width (HPBW) at 3 mm ranges from  $\sim 31''$  to  $\sim 21''$  (see Table A.1). We reduced and analyzed the data using the GILDAS software,<sup>1</sup> as described in Cuadrado et al. (2015). The rms noise obtained after 4 h – 5 h integrations is typically  $\sim 1 \text{ mK} - 5 \text{ mK}$  per resolution channel. The antenna temperature,  $T_A^*$ , was converted to the main beam temperature,  $T_{\text{MB}}$ , through the  $T_{\text{MB}} = T_A^*/\eta_{\text{MB}}$  relation, where  $\eta_{\text{MB}}$  is the antenna efficiency, which is defined as the ratio between main beam efficiency,  $B_{\text{eff}}$ , and forward efficiency,  $F_{\text{eff}}^2$ . All line intensities in figures and tables are in units of main beam temperature.

<sup>1</sup> <http://www.iram.fr/IRAMFR/GILDAS/>

<sup>2</sup> <http://www.iram.es/IRAMES/mainWiki/Iram30mEfficiencies>

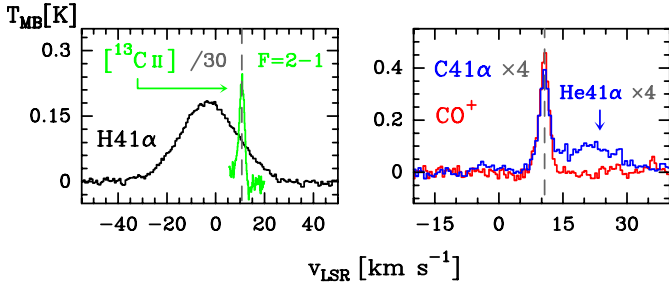


**Fig. 2.** Line profiles toward the Orion Bar (DF position). *Left:* H41 $\alpha$  with  $\Delta v \approx 26 \text{ km s}^{-1}$  and  $v_{\text{LSR}} \approx -4 \text{ km s}^{-1}$ , and [ $^{13}\text{C II}$ ] (intensity divided by 30) with  $\Delta v \approx 2.6 \text{ km s}^{-1}$  (the [ $^{12}\text{C II}$ ] emission has been blanked out). *Right:* CO $^+$   $N, F = 2, 5/2 - 1, 3/2$  and C41 $\alpha$  lines with  $\Delta v \approx 2.6 \text{ km s}^{-1}$ . Dashed lines indicate the LSR velocity,  $10.7 \text{ km s}^{-1}$ , of the PDR.

The intensities of the  $Cn\alpha$  lines were extracted from a two-Gaussian fit to each observed feature: one narrow Gaussian for the  $Cn\alpha$  lines, and a broader one for the  $Hen\alpha$  lines (see fits in Fig. A.1). With these fits we determined the contribution,  $\approx 40\%$ , of the  $Hen\alpha$  line wings to the observed emission at  $Cn\alpha$  velocities. We used this value to estimate the contribution of the putative  $Hen\beta$  and  $Hen\gamma$  line wings to the faint  $Cn\beta$  and  $Cn\gamma$  lines. We conclude that the uncertainty (calibration and line overlap) of our mmCRL intensities is  $\approx 15\%$ . The resulting mmCRL spectroscopic parameters are given in Table A.1.

We also made use of the [ $^{13}\text{C II}$ ] map taken by Herschel/HIFI toward OMC-1 (Goicoechea et al. 2015). We analyzed the strongest, yet optically thin, [ $^{13}\text{C II}$ ]  $F = 2 - 1$  hyperfine emission component at 1900.466 GHz (red contours in Fig. 1). To make a comparison with the mmCRLs, we smoothed the map to an angular resolution of  $\sim 25''$  and extracted the [ $^{13}\text{C II}$ ] ( $F = 2 - 1$ ) integrated line intensity,  $20 \pm 3 \text{ K km s}^{-1}$ , toward the DF.

### 3. Results

Figure 1 shows the observed positions over a map of the optically thin  $^{13}\text{CO}$  ( $J = 3 - 2$ ) and [ $^{13}\text{C II}$ ] ( $^2P_{3/2} - ^2P_{1/2}, F = 2 - 1$ ) emission lines along the Bar. We detect 12 mmCRLs toward the DF: C42 $\alpha$  to C38 $\alpha$ , C52 $\beta$  to C48 $\beta$ , and C60 $\gamma$  to C59 $\gamma$ . All lines are shown in Fig. A.1 of the Appendix. The emission from these lines gets fainter as we go from the DF to the more shielded molecular gas, thus mmCRLs trace the FUV-irradiated edge of the molecular cloud. The  $Cn\alpha$  lines show an emission shoulder shifted by  $\approx +10 \text{ km s}^{-1}$ . This feature is produced by He recombination lines ( $IP = 24.6 \text{ eV}$ ). Helium lines do not arise from the neutral PDR; they are emitted from the surrounding ‘Huygens’ H II region and from foreground layers of ionized gas that extend all the way to the edge of Orion’s Veil (see, e.g., Rubin et al. 2011; O’Dell et al. 2017; Pabst et al. 2019).

The observed mmCRLs have line profiles that are very different from those of H and He recombination lines (Fig. 2). The H and He recombination lines show much broader line widths ( $\Delta v = 10 - 30 \text{ km s}^{-1}$ ) produced by the high electron temperatures and pressures of the fully ionized gas. They peak at  $v_{\text{LSR}} = -2$  to  $-11 \text{ km s}^{-1}$ , consistent with ionized gas that flows toward the observer. Carbon recombination lines, however, peak at  $v_{\text{LSR}} = +10.7 \pm 0.2 \text{ km s}^{-1}$  and show narrow line profiles,  $\Delta v = 2.6 \pm 0.4 \text{ km s}^{-1}$ . These values are nearly identical to those displayed by [ $^{13}\text{C II}$ ] and by molecular lines observed toward the DF position at comparable angular resolution (e.g., Cuadrado et al. 2015). In particular, mmCRLs and [ $^{13}\text{C II}$ ]

line profiles are analogous to those of HOC $^+$  and CO $^+$  (Fig. 2). These reactive molecular ions form by chemical reactions involving C $^+$  with H $_2$ O and OH, respectively (e.g., Fuente et al. 2003; Goicoechea et al. 2017). Hence, they likely trace the same gas component.

For optically thin emission, line widths are determined by thermal broadening ( $\propto \sqrt{T_k}$ ) and by nonthermal broadening produced by gas turbulence and macroscopic motions in the PDR. Adopting a nonthermal velocity dispersion<sup>3</sup> of  $\sigma_{\text{nth}} = 1.0 \pm 0.1 \text{ km s}^{-1}$  ( $\Delta v_{\text{nth}} = 2.355 \cdot \sigma_{\text{nth}}$ ), the observed mmCRL widths imply a beam-averaged gas temperature of  $T_k = 450^{+280}_{-300} \text{ K}$ . The [ $\text{C II}$ ] 158  $\mu\text{m}$  line shows a broader line width,  $\Delta v = 4.1 \pm 0.1 \text{ km s}^{-1}$ , toward the DF. Because the line emission is moderately optically thick ( $\tau_{[\text{C II}]} \approx 1 - 2$ ; see Ossenkopf et al. 2013; Goicoechea et al. 2015), these line width differences are, at least in part, produced by opacity-broadening of the [ $\text{C II}$ ] 158  $\mu\text{m}$  line. However, Ossenkopf et al. (2013) pointed out that opacity-broadening alone does not fully explain the broader [ $\text{C II}$ ] line profile compared to [ $^{13}\text{C II}$ ]. These line width differences may suggest that, in comparison to [ $^{13}\text{C II}$ ] and mmCRLs, the [ $\text{C II}$ ] 158  $\mu\text{m}$  emission has a significant contribution from hotter gas in the mostly atomic PDR ( $x_{\text{H}} > x_{\text{H}_2}$ ), thus closer to the ionization front (the PDR/H II interface).

### 4. Analysis

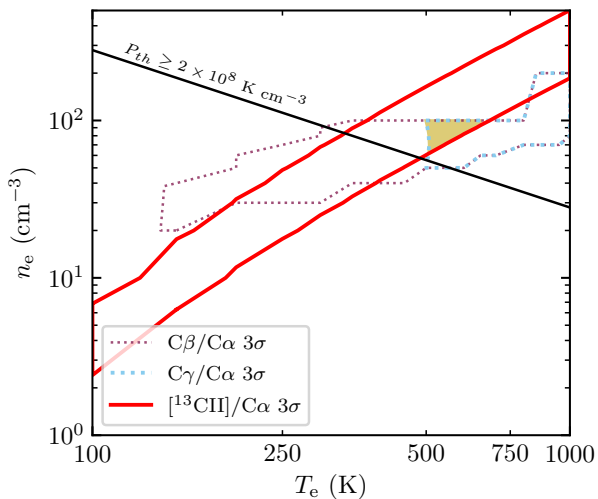
Our 3 mm-wave observations have allowed us to detect several  $\alpha$ ,  $\beta$ , and  $\gamma$  CRLs toward the Bar. The observed  $n$  dependence of their line strengths is determined by the level populations. These can be modeled and used to derive  $n_e$  and  $T_e$  (see theory in e.g., Walmsley & Watson 1982; Salgado et al. 2017).

Figure 3 shows results of a grid of non-LTE<sup>4</sup> excitation models for  $n_e$  ranging from  $1 \text{ cm}^{-3}$  to  $500 \text{ cm}^{-3}$ , and  $T_e$  ranging from 100 K to 1000 K. Our models use non-LTE level populations computed by Salgado et al. (2017) without a background radiation field. Models assume that the observed lines are optically thin (for the conditions prevailing in the Bar, we determine that the opacity of the C41 $\alpha$  line is  $\tau \approx 10^{-2}$ ). Our models also compute the [ $^{13}\text{C II}$ ]  $^2P_{3/2} - ^2P_{1/2}$  excitation, and use the [ $^{12}\text{C}/^{13}\text{C}$ ]  $\approx 67$  isotopic abundance ratio inferred in Orion (Langer et al. 1984). The colored area in Fig. 3 shows the best models fitting line intensity ratios that include all<sup>5</sup> observed  $\alpha$ ,  $\beta$ , and  $\gamma$  mmCRLs and [ $^{13}\text{C II}$ ]. The black line shows where the gas thermal pressure ( $P_{\text{th}} = n_{\text{H}} \cdot T_k$ ) is  $2 \cdot 10^8 \text{ cm}^{-3} \text{ K}$ . To plot this line we assume  $x_e = x_{\text{C}^+} = [\text{C}/\text{H}]$ ; in other words, all free electrons come from the ionization of carbon atoms, with an gas-phase abundance of  $[\text{C}/\text{H}] = 1.4 \cdot 10^{-4}$  with respect to H nuclei in Orion (Sofia et al. 2004). Absolute line intensity predictions depend on the assumed path-length  $l$  along the line of sight. The  $\sim 25''$  beam-averaged C $^+$  column density,  $N(\text{C}^+)$ , estimated from [ $^{13}\text{C II}$ ] is  $N(\text{C}^+) \approx 10^{19} \text{ cm}^{-2}$  (Goicoechea et al. 2015). Assuming a representative density of  $n_{\text{H}} \approx 10^5 \text{ cm}^{-3}$  in

<sup>3</sup> Calculated from detailed nonlocal radiative transfer models of the molecular line emission toward the DF (Goicoechea et al. 2016, 2017).

<sup>4</sup> The observed mmCRL intensity ratios approach LTE for  $T_e \gtrsim 500 \text{ K}$ . Assuming LTE excitation results in mmCRL intensities brighter by  $\lesssim 25\%$ . Hence, the estimated  $n_e$  in LTE are  $\lesssim 25\%$  lower.

<sup>5</sup> The properties of the observed  $\alpha$ ,  $\beta$ , and  $\gamma$  carbon recombination lines vary slowly with  $n$ . In order to increase the statistical significance of our comparison between models and observations, we used the inverse-variance weighted intensity averages of the observed  $Cn\alpha$  ( $n$  from 38 to 42),  $Cn\beta$  ( $n$  from 48 to 52), and  $Cn\gamma$  ( $n$  from 59 to 60) lines.



**Fig. 3.** Constraints on  $n_e$  and  $T_e$  toward the Orion Bar DF from non-LTE excitation models that assume a path length of  $0.02 \leq l \leq 0.2$  pc. The colored area shows the overlap region of models for different line intensity ratios (within a  $3\sigma$  uncertainty range in the observed ratios).

the atomic PDR (Tielens et al. 1993), the inferred  $N(\text{C}^+)$  is equivalent to  $l \approx 0.2$  pc. This is consistent with other estimations based on the infrared dust emission ( $l = 0.28 \pm 0.06$  pc, Salgado et al. 2016). If the gas density is a factor of ten higher (e.g., Andree-Labsch et al. 2017) then  $l \approx 0.02$  pc.

Our absolute intensity and line ratio models restrict  $n_e$  and  $T_e$  toward the DF position to  $60\text{--}100\text{ cm}^{-3}$  and  $500\text{--}600$  K, respectively. The inferred electron temperatures in the colored area of Fig. 3 fall within the thermal line widths derived from the observed mmCRL profiles (see previous section). Assuming<sup>6</sup>  $x_e \leq 1.4 \cdot 10^{-4}$ , the derived electron densities are equivalent to gas densities of  $n_{\text{H}} \geq (4\text{--}7) \cdot 10^5\text{ cm}^{-3}$ . Thus, gas thermal pressures of  $P_{\text{th}} \geq (2\text{--}4) \cdot 10^8\text{ cm}^{-3}\text{ K}$  toward the DF.

## 5. Discussion and prospects

Using mmCRL observations and models, we inferred  $n_e = 60\text{--}100\text{ cm}^{-3}$  at the  $\text{H}/\text{H}_2$  dissociation front of the Orion Bar PDR. These electron densities are higher than the  $\approx 10\text{ cm}^{-3}$  values typically used in molecular excitation models of the region (e.g., van der Tak et al. 2012, 2013). In addition, by assuming  $x_e \leq 1.4 \cdot 10^{-4}$ , we estimated a lower limit<sup>6</sup> to  $P_{\text{th}}$  in the DF. The high inferred gas thermal pressures confirm earlier estimations based on the analysis of ALMA images of the molecular gas emission (Goicoechea et al. 2016, 2017) and of Herschel observations of specific tracers of the DF (e.g., high- $J$  CO and  $\text{CH}^+$  rotational lines; Nagy et al. 2013; Joblin et al. 2018). Nonstationary photoevaporating PDR models (e.g., Bertoldi & Draine 1996; Bron et al. 2019) predict such high pressures in PDRs. In these time-dependent models, the strong stellar FUV field heats, compresses, and gradually evaporates the molecular cloud edge if the pressure of the surrounding medium (the adjacent  $\text{H II}$  region) is not significantly higher. The derived thermal pressure toward the DF,  $P_{\text{th}} \geq 2 \cdot 10^8\text{ cm}^{-3}\text{ K}$ , is indeed higher than that of the ionized

<sup>6</sup> Our inferred  $n_{\text{H}}$  and  $P_{\text{th}}$  values are lower limits if mmCRLs arise from PDR gas layers where a significant fraction of carbon is not locked in  $\text{C}^+$ , and thus  $x_e < 1.4 \cdot 10^{-4}$  and  $x_e > x(\text{C}^+)$ .

gas at the ionization front ( $\approx 6 \cdot 10^7\text{ cm}^{-3}\text{ K}$ , Walmsley et al. 2000) and, in contrast to previous indirect studies of the pressure in the Bar (Pellegrini et al. 2009), leaves little room for magnetic pressure support. This conclusion is in line with the relatively modest plane-of-the-sky magnetic field strength reported from far-IR polarimetric observations with SOFIA/HAWC+ (Chuss et al. 2019).

Unfortunately, the  $\sim 25''$  resolution of our single-dish observations does not allow us to spatially resolve the  $[\text{C II}]$  and mm-CRLs emitting layers. We note that  $A_{\text{V}} = 1$ , roughly the width of the  $\text{H}/\text{H}_2$  transition layer, implies  $3.2''\text{--}1.6''$  for  $n_{\text{H}} = 10^5$  and  $10^6\text{ cm}^{-3}$ , respectively. The  $\sim 10''$  resolution VLA map of the  $\text{C}91\alpha$  line (Wyrowski et al. 1997) shows that the  $\text{C}^+$  gas layer seen in this CRL is spatially coincident with the IR emission from  $\text{H}_2^*$  that traces the  $\text{H}/\text{H}_2$  dissociation front (shown in Fig. 1). This result is somewhat surprising because constant-density stationary PDR models have long predicted that the  $\text{C}^+/\text{C}/\text{CO}$  transition in the Bar should be located deeper inside the cloud, and separated from the DF by several arcsec (e.g., Tielens et al. 1993). In addition, single-dish observations show that the  $[\text{C I}]$  492 GHz emission spatially correlates with that of  $^{13}\text{CO}$  ( $J = 2\text{--}1$ ) (Tauber et al. 1995). This suggests that the classical  $\text{C}^+/\text{C}/\text{CO}$  sandwich structure of a PDR may not be discernible, or even exist, in the sense that there would be no layer in the Bar where neutral atomic carbon is the most abundant carbon reservoir. Indeed, ALMA images of the Bar at  $\approx 1''$  resolution show that there is also no appreciable offset between the  $\text{H}_2^*$  emission and the edge of the  $\text{HCO}^+$  and CO emission (Goicoechea et al. 2016). All these new observations thus suggest that we still do not fully understand the properties and exact location of the  $\text{C}^+/\text{C}/\text{CO}$  transition in interstellar clouds.

In this work we provided evidence that the electron density at the edge of the Orion Bar PDR is quite high, and this may have consequences for the coupling of matter with the magnetic field and the excitation of certain molecules. Much higher resolution ALMA observations of mmCRLs and of neutral atomic carbon  $[\text{C I}]$  fine-structure lines are clearly needed to spatially resolve these critical interface layers of the ISM.

*Acknowledgements.* We thank the Spanish MICIU for funding support under grant AYA2017-85111-P and the ERC for support under grant ERC-2013-SyG-610256-NANOCOSMOS. A.B.-R. also acknowledges support by the MICIU and FEDER funding under grants ESP2015-65597-C4-1-R and ESP2017-86582-C4-1-R. P.S. and A.G.G.M.T. acknowledge financial support from the Dutch Science Organisation through TOP grant 614.001.351.

## References

- Andree-Labsch, S., Ossenkopf-Okada, V., & Röllig, M. 2017, *A&A*, 598, A2  
 Bakes, E. L. O. & Tielens, A. G. G. M. 1994, *ApJ*, 427, 822  
 Bertoldi, F. & Draine, B. T. 1996, *ApJ*, 458, 222  
 Bron, E., Agúndez, M., Goicoechea, J. R., & Cernicharo, J. 2019, arXiv e-prints  
 Caselli, P., Walmsley, C. M., Terzieva, R., & Herbst, E. 1998, *ApJ*, 499, 234  
 Churchwell, E., Smith, L. F., Mathis, J., Mezger, P. G., & Huchtmeier, W. 1978, *A&A*, 70, 719  
 Chuss, D. T., Andersson, B.-G., Bally, J., et al. 2019, *ApJ*, 872, 187  
 Cuadrado, S., Goicoechea, J. R., Cernicharo, J., et al. 2017, *A&A*, 603, A124  
 Cuadrado, S., Goicoechea, J. R., Pilleri, P., et al. 2015, *A&A*, 575, A82  
 Cuadrado, S., Goicoechea, J. R., Roncero, O., et al. 2016, *A&A*, 596, L1  
 Fuente, A., Rodríguez-Franco, A., García-Burillo, S., Martín-Pintado, J., & Black, J. H. 2003, *A&A*, 406, 899  
 Goicoechea, J. R., Cuadrado, S., Pety, J., et al. 2017, *A&A*, 601, L9  
 Goicoechea, J. R., Pety, J., Cuadrado, S., et al. 2016, *Nature*, 537, 207  
 Goicoechea, J. R., Pety, J., Gerin, M., et al. 2009, *A&A*, 498, 771  
 Goicoechea, J. R., Santa-Maria, M. G., Bron, E., et al. 2019, *A&A*, 622, A91  
 Goicoechea, J. R., Teyssier, D., Etxaluze, M., et al. 2015, *ApJ*, 812, 75  
 Goldsmith, P. F. & Kauffmann, J. 2017, *ApJ*, 841, 25  
 Goldsmith, P. F., Langer, W. D., Pineda, J. L., & Velusamy, T. 2012, *ApJS*, 203,

- Guelin, M., Langer, W. D., & Wilson, R. W. 1982, *A&A*, 107, 107  
Herbst, E. & Klemperer, W. 1973, *ApJ*, 185, 505  
Hollenbach, D. J. & Tielens, A. G. G. M. 1999, *RevModPhys.*, 71, 173  
Joblin, C., Bron, E., Pinto, C., et al. 2018, *A&A*, 615, A129  
Kaufman, M. J., Wolfire, M. G., & Hollenbach, D. J. 2006, *ApJ*, 644, 283  
Langer, W. D., Gaeddel, T. E., Frerking, M. A., & Armentrout, P. B. 1984, *ApJ*, 277, 581  
Maret, S. & Bergin, E. A. 2007, *ApJ*, 664, 956  
Nagy, Z., Van der Tak, F. F. S., Ossenkopf, V., et al. 2013, *A&A*, 550, A96  
Natta, A., Walmsley, C. M., & Tielens, A. G. G. M. 1994, *ApJ*, 428, 209  
O'Dell, C. R. 2001, *ARA&A*, 39, 99  
O'Dell, C. R., Kollatschny, W., & Ferland, G. J. 2017, *ApJ*, 837, 151  
Oppenheimer, M. & Dalgarno, A. 1974, *ApJ*, 192, 29  
Ossenkopf, V., Röllig, M., Neufeld, D. A., et al. 2013, *A&A*, 550, A57  
Pabst, C., Higgins, R., Goicoechea, J. R., et al. 2019, *Nature*, 565, 618  
Pankonin, V. & Walmsley, C. M. 1978, *A&A*, 67, 129  
Pellegrini, E. W., Baldwin, J. A., Ferland, G. J., et al. 2009, *ApJ*, 693, 285  
Pety, J., Guzmán, V. V., Orkisz, J. H., et al. 2017, *A&A*, 599, A98  
Rubin, R. H., Simpson, J. P., Haas, M. R., & Erickson, E. F. 1991, *ApJ*, 374, 564  
Rubin, R. H., Simpson, J. P., O'Dell, C. R., et al. 2011, *MNRAS*, 410, 1320  
Salas, P., Oonk, J. B. R., van Weeren, R. J., et al. 2018, *MNRAS*, 475, 2496  
Salgado, F., Berné, O., Adams, J. D., et al. 2016, *ApJ*, 830, 118  
Salgado, F., Morabito, L. K., Oonk, J. B. R., et al. 2017, *ApJ*, 837, 141  
Sofía, U. J., Lauroesch, J. T., Meyer, D. M., & Cartledge, S. I. B. 2004, *ApJ*, 605, 272  
Stoerzer, H., Stutzki, J., & Sternberg, A. 1995, *A&A*, 296, L9  
Tauber, J. A., Lis, D. C., Keene, J., Schilke, P., & Büttgenbach, T. H. 1995, *A&A*, 297, 567  
Tielens, A. G. G. M., Meixner, M. M., van der Werf, P. P., et al. 1993, *Science*, 262, 86  
van der Tak, F. F. S., Nagy, Z., Ossenkopf, V., et al. 2013, *A&A*, 560, A95  
van der Tak, F. F. S., Ossenkopf, V., Nagy, Z., et al. 2012, *A&A*, 537, L10  
Walmsley, C. M., Natta, A., Oliva, E., & Testi, L. 2000, *A&A*, 364, 301  
Walmsley, C. M. & Watson, W. D. 1982, *ApJ*, 260, 317  
Wyrowski, F., Schilke, P., Hofner, P., & Walmsley, C. M. 1997, *ApJ*, 487, L171

## Appendix A: Tables and figures

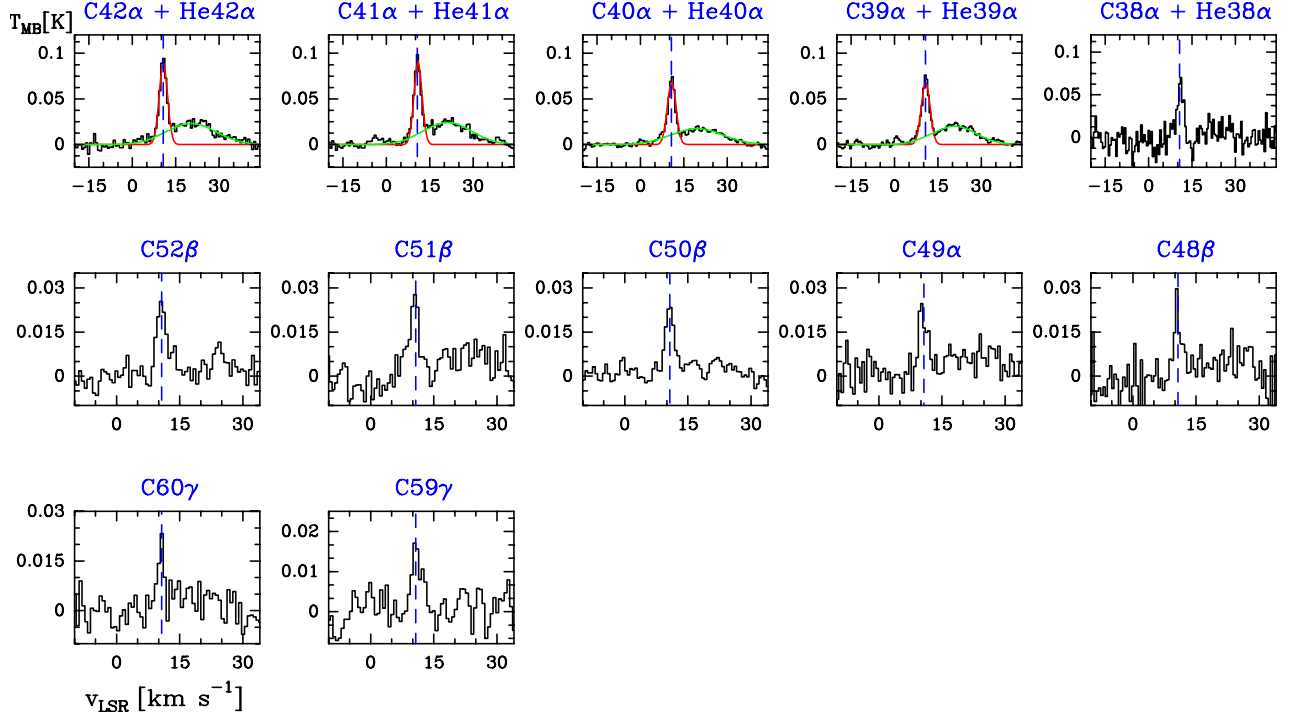


**Fig. A.1.** Carbon recombination lines between 80 GHz and 116 GHz detected with the IRAM 30 m telescope toward the Orion Bar (DF position). The dashed lines indicate the LSR velocity ( $10.7 \text{ km s}^{-1}$ ) of the molecular gas in the PDR. The red and green curves show Gaussian fits to the  $Cn\alpha$  and  $He n\alpha$  lines, respectively. We use these fits to determine the contribution of He recombination line wings to the emission observed in the velocity range of the  $Cn\beta$  and  $Cn\gamma$  lines. We note the different abscissa and ordinate axis scales.

**Table A.1.** Line spectroscopic parameters obtained from Gaussian fits to the observed mmCRLs (see Sect. 2).

Line	Frequency [MHz]	$\int T_{\text{MB}} dv^{a,b}$ [mK km s <sup>-1</sup> ]	$v_{\text{LSR}}^b$ [km s <sup>-1</sup> ]	$\Delta v^b$ [km s <sup>-1</sup> ]	$T_{\text{MB}}^a$ [mK]	$S/N^c$	HPBW <sup>d</sup> [arcsec]
C42 $\alpha$	85731.14	226.8 (10.5)	10.6 (0.1)	2.6 (0.1)	83.1	21	28.7
C41 $\alpha$	92080.35	248.9 (14.2)	10.8 (0.1)	2.7 (0.1)	85.6	17	26.7
C40 $\alpha$	99072.36	172.6 (7.2)	10.7 (0.1)	2.5 (0.1)	63.6	23	24.8
C39 $\alpha$	106790.61	190.9 (13.3)	10.7 (0.1)	2.9 (0.2)	53.5	12	23.0
C38 $\alpha$	115331.91	163.9 (19.6)	10.9 (0.2)	2.4 (0.3)	65.4	5	21.3
C52 $\beta$	88449.80	53.8 (9.4)	10.7 (0.2)	2.9 (0.5)	24.5	6	27.8
C51 $\beta$	93654.02	55.2 (8.3)	10.5 (0.2)	2.9 (0.6)	24.8	6	26.3
C50 $\beta$	99274.72	47.7 (6.0)	10.7 (0.1)	2.7 (0.3)	23.6	8	24.8
C49 $\beta$	105354.40	42.4 (8.5)	10.6 (0.2)	2.6 (0.5)	21.5	4	23.3
C48 $\beta$	111940.89	36.9 (11.0)	10.6 (0.2)	2.3 (0.6)	21.8	4	22.0
C60 $\gamma$	84956.76	27.8 (8.2)	10.5 (0.2)	1.7 (0.5)	22.3	5	29.0
C59 $\gamma$	89243.05	35.1 (8.3)	10.9 (0.3)	3.0 (0.6)	15.4	4	27.6

**Notes.** <sup>a</sup> Intensities in main beam temperature (in units of mK). <sup>b</sup> Parentheses indicate the uncertainty obtained by the Gaussian fitting routine. <sup>c</sup> Signal-to-noise ratio with respect to the peak line temperature in velocity resolution channels of 0.7 km s<sup>-1</sup>. <sup>d</sup> The half power beam width (HPBW) of the IRAM 30 m telescope is well described by  $\text{HPBW}[\text{arcsec}] \approx 2460/\text{Frequency}[\text{GHz}]$ .